High-Efficiency Perovskite Solar Cell Based on Sequential Doping of PTAA

Yangyi Yao, Wei-Lun Hsu, and Mario Dagenais

***Abstract*—Perovskite solar cells have been extensively studied and have recently demonstrated a power conversion efficiency above 23%. In our present approach, we select poly(triaryl amine) (PTAA) as the hole-transport material and use an inverted solar cell planar structure. We propose a sequential method to dope the PTAA thin film in order to reduce the solar cell's series resistance. A modified inter-diffusion method is adopted to improve the perovskite film. We optimize the solvent-assisted annealing condition to maximize the perovskite grain size and reduce the pin-hole density. The impact of PTAA's doping concentration on the solar cell's PV performance is investigated. Compared to conventional PEDOT:PSS-based perovskite solar cell, we observe an improvement in both the open-circuit voltage and the short-circuit current, resulting in a power conversion efficiency enhancement from 12.7% to 15.3%.**

***Index Terms*—Doping, efficiency, grain size, perovskite solar cell, sequential method.**

I. Introduction

ORGANOMETAL halide perovskite solar cells have already demonstrated remarkable power conversion efficiency (PCE) enhancement from 3.8% [1] in 2009 to 23.7% [2] in late 2018. The active perovskite material has evolved from methylammonium lead iodide to the complex mixed halide compound $(\mathrm{CsI})_x(\mathrm{FAI})_{1-x}\mathrm{PbBr}_y\mathrm{I}_{1-y}$ following the discovery of improved light absorption and stability when using formamidinium-based perovskite materials [3]. On the other hand, methylammonium lead halide is still the dominant material being used today in most perovskite solar cell research since their active layer has remarkable properties, such as long carrier diffusion length [4], large carrier mobility [5], tunable bandgap [6], and low-temperature solution processability. There are two dominant structures for the perovskite solar cell: the meso-porous (n-i-p) structure and the inverted (p-i-n) planar structure. The meso-porous structure usually requires a high-temperature-annealing condensed base layer to minimize the leakage paths from the perovskite layer to the conducting layer [7]–[10]. Yang *et al.* from UNIST achieved 22.1% PCE with the conventional $\mathrm{TiO_2}$ based structure in 2017 [10]. On the other hand, the inverted planar perovskite structure simplifies the fabrication procedure without sacrificing too much PCE. Recently, Luo *et al.* reported 21% PCE with an inverted structure using a mixed-cation lead mixed-halide perovskite material [11]. In contrast with the conventional $\mathrm{TiO_2}$-based mesa-porous perovskite structure, there are many candidates for the base hole-transport material (HTM) in an inverted planar structure. Inorganic materials such as $\mathrm{NiO_x}$ [12], [13] and CuI [14], [15] have been considered as the HTM in planar perovskite solar cell. Recently, doped $\mathrm{NiO_x}$ has attracted attention, Chen has focused on the doping technique in $\mathrm{NiO_x}$ and has reported ~20% PCE using different dopants such as Cu and Cs [16]–[18]. Compared with inorganic HTMs, organic HTMs are widely adopted for better film coverage and easier control of doping levels. PEDOT:PSS is a popular HTM for its high conductivity and low cost, but its relatively lower work function, which leads to a band mismatch with the perovskite material, usually results in smaller open-circuit voltage (~0.9 V) [19]–[23]. Various organic HTMs have been extensively studied for better band alignment, however many of them are not compatible with the inverted structure. For example, the Spiro-MeOTAD cannot be used as the base HTM because of its high solubility in N, N-dimethyl formamide (DMF) and dimethyl sulfoxide (DMSO) (general solvent for perovskite). It is easy to be washed away when spin-coating a perovskite precursor solution on it. Conducting polymers like poly [N,N'-bis(4-butylphenyl)-N,N'-bis(phenyl)benzidine] (poly-TPD) [24]–[26] and poly(triaryl amine) (PTAA) [27]–[29] are good candidates because of their resistance to DMF and DMSO wash. But the non-wetting nature of their surfaces is the main challenge for top perovskite film growth, resulting in poor perovskite film coverage, increased pin-hole density, and relatively small perovskite grain size. It has been demonstrated that the perovskite grain size is highly dependent on the hydrophobicity of the bottom layer surface [27], and that larger grain size can be obtained on better hydrophilic HTM surfaces. Recently there have been several breakthroughs in the conducting polymer HTM studies. Xu *et al.* have reported that poly-TPD-based inverted planar perovskite solar cell can have a PCE exceeding 18% [26]. They resolved the problem of the non-wetting nature of poly-TPD by using ultraviolet-ozone surface modification. Huang *et al.* have proposed to use doped PTAA thin film as the base HTM to reduce the series resistance and recently they boosted the efficiency from 17.5% [28] to 20.6% [29]. In their approach, PTAA solution is mixed with F4-TCNQ as the doping material and m-MTDATA is used as the surface modification material.

Manuscript received February 14, 2019; accepted March 24, 2019. Date of publication May 6, 2019; date of current version June 19, 2019. This work was supported by the National Science Foundation under Grant 1665449. *(Corresponding author: Mario Dagenais.)*

The authors are with the Department of Electrical and Computer Engineering, University of Maryland, College Park, MD 20742 USA (e-mail: yyao123@umd.edu; allanhsu@umd.edu; dage@ece.umd.edu).

Color versions of one or more of the figures in this paper are available online at http://ieeexplore.ieee.org.

Digital Object Identifier 10.1109/JPHOTOV.2019.2910236

In our study, we focus on the simple PTAA-based planar perovskite solar cell without using a complicated surface passivation technique. We propose a sequential method to dope PTAA in an easier and more stable way. Considering the conventional polymer:F4-TCNQ blend solution, it is observed that this doping material often results in drastically reduced solubility of polymers. As a result of this, the mixed solutions must be kept at high temperature and diluted concentrations to avoid rapid aggregation [30]. In addition, we observe the rapid degradation of F4-TCNQ in a mixed PTAA solution with an obvious color change within a few days, which definitely induces more uncertainties in device performance and solution preparation. To minimize the above-mentioned drawbacks, we propose a sequential method to dope PTAA by exposing the PTAA film to the doping solution in an orthogonal solvent system, i.e., toluene for PTAA and 2-propanol for F4-TCNQ. It is found that the PTAA's doping level can be tuned by the concentration of the doping solution. This sequential method improves the device's reproducibility and long-term sustainability. In our work, we have also modified the inter-diffusion method [31] with a controlled solvent-assisted annealing approach to grow high-quality perovskite thin film with large grain size (over 2 μm). The optimized recipe guarantees the successful formation of a perovskite layer with average thickness greater than 400 nm without any PbI_2 residue. In this paper, we demonstrate a perovskite solar cell with a simple planar structure of FTO/PTAA/$CH_3NH_3PbI_3$/phenyl-C61-butyric acid methyl ester (PCBM)/Ag and we achieve a champion PCE of 15.3% based on the sequentially doped PTAA thin film without using a complicated surface passivation technique.

II. EXPERIMENTAL SECTION

A. Materials

Fluorine doped tin oxide (FTO) glass and methylammonium bromide (MABr) solution were purchased from Sigma Aldrich. Methylammonium iodide (MAI), poly[bis(4-phenyl)(2,4,6-trimethylphenyl)amine] (PTAA), 2,3,5,6-tetrafluoro-7,7,8,8-tetracyanoquinodimethane (F4-TCNQ), PCBM, and 4,4',4"-tris(3-methylphenylphenylamino)triphenylamine) (m-MTD ATA) were obtained from Lumtec. Lead iodide (PbI_2), anhydrous DMF, toluene, 2-propanol, and chlorobenzene were purchased from Alfa Aesar.

B. Device Fabrication

The perovskite solar cell fabrication procedure is shown in Fig. 1(a). The FTO glass is first cleaned with acetone, methanol, isopropanol, and deionized water in an ultrasonic bath successively. Prior to any device fabrication, the cleaned substrates undergo an ultraviolet-ozone (UVO) exposure treatment for 20 min to remove any organic residues. After UVO treatment, the substrate is transferred into the nitrogen filled glove box and preheated at 100 °C on a hot plate. Then, 20 μl hot PTAA solution (2 mg/ml in toluene with 10 wt% ratio of m-MTDATA additive) is spin-coated on the hot substrate at 3240 r/min for 45 s, followed with 10 min drying at 100 °C. After cooling down the substrate to room temperature, the F4-TCNQ solution (1 mg/ml in 2-propanol) is dropped on the PTAA surface and left for 30 s before spin-drying at 4260 r/min for 45 s. The doped PTAA film preparation is completed after 10 min annealing at 100 °C. The modified inter-diffusion method is utilized here to grow the perovskite layer. Specifically, high-concentrated hot PbI_2 solution (500 mg/ml in DMF) is spin-coated on doped PTAA surface at 3000 r/min for 30 s, followed by 10 min annealing at 85 °C to crystalize PbI_2; then a hot MAI solution (75 mg/ml in 2-propanol) is sequentially spin-coated on the PbI_2 layer at 2000 r/min for 2 min. The color changes from shiny yellow to dark brown immediately when MAI reaches the PbI_2 surface. About 30 μl toluene is dropped for the last 30 s of the MAI spin-coating period to wash away the MAI residue and passivate the perovskite surface. The pre-crystallized perovskite layer is then moved into a self-built vapor environment as shown in Fig. 1(b) for solvent-assisted annealing at 150 °C for 1 h. After that, a small amount of MABr solution (4 mg/ml in 2-propanol) is spin-coated on a room temperature perovskite surface for post passivation treatment. To grow the electron-transport layer, a 20 μl hot PCBM solution (20 mg/ml in chlorobenzene) is spin-coated at 4000 r/min for 30 s, followed by 10 min annealing at 100 °C. Finally, the sample is transferred into the e-beam evaporator for the deposition of the Ag top contacts using a shadow masks to define the effective device area.

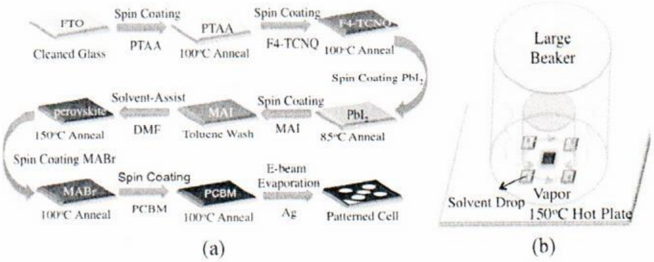

Fig. 1. (a) Fabrication procedure of perovskite solar cell. (b) Solvent-assisted vapor annealing set-up.

C. Device Characterization

We use a Newport Model 91159 Full Spectrum 150 W Solar Simulator as the light source to evaluate the solar cells performance with an Air Mass 1.5 filter. It is calibrated by a KG-5 Si diode to produce a 1-sun light illumination. The *I–V* characteristics of the perovskite solar cell is measured in ambient with the Keithley 2400 source-meter. The X-ray diffraction (XRD) patterns are acquired on a Bruker D8/C2 Discover Parallel Beam Diffractometer using Cu Kα radiation. The scanning electron microscope (SEM) images are taken by a Hitachi SU-70 Schottky Field Emission Gun Scanning Electron Microscope. The atomic force microscope (AFM) images are obtained from an MFP-3D Origin AFM (Asylum Research). The external quantum efficiency is measured with a self-build photo-spectrometer system. The sample area is illuminated with a modulated monochromatic light beam (Xe light source), and the detected photocurrent is locked and amplified with a

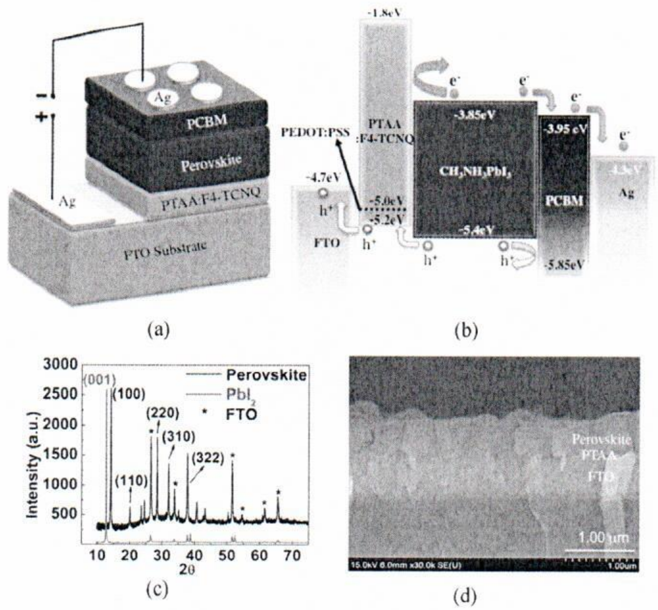

Fig. 2. (a) Perovskite solar cell planar structure. (b) Energy band diagram. (c) XRD pattern of PbI_2 film and annealed perovskite film. (d) Cross-sectional SEM image of FTO/PTAA/perovskite.

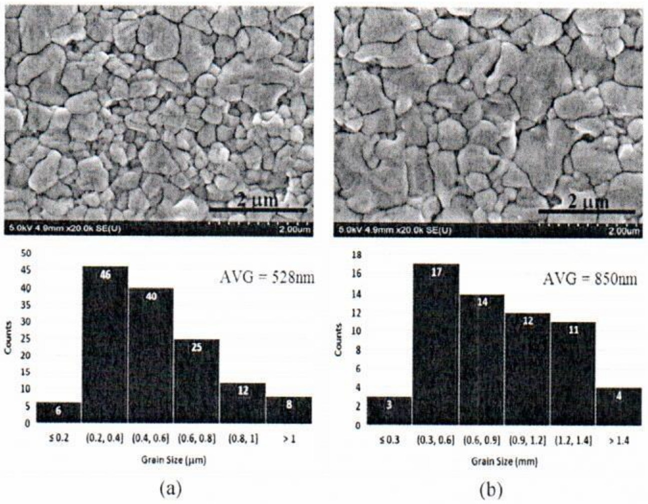

Fig. 3. (a) SEM image of the perovskite thin film grown on PEDOT:PSS and its grain size distribution histogram. (b) SEM image of the perovskite grown on PTAA base and the corresponding grain size distribution histogram.

Stanford Research Systems SR830 lock-in amplifier and a Stanford Research Systems SR570 pre-amplifier, respectively.

III. Results and Analysis

This study aims to achieve high-performance inverted planar perovskite solar cell with the sequentially doped PTAA hole-transport layer. Fig. 2(a) shows the solar cell structure of FTO/PTAA:F4-TCNQ/$CH_3NH_3PbI_3$/PCBM/Ag and Fig. 2(b) is the corresponding energy band diagram. We choose PTAA as the base HTM instead of PEDOT:PSS to enhance the solar cell performance mainly by increasing the open-circuit voltage (*V*oc). PEDOT:PSS is widely used as a high conductivity and low-cost HTM in the inverted planar perovskite solar cell. However, these solar cells usually suffer from low *V*oc ($\sim$0.9 V) due to energy level mismatch between PEDOT:PSS and perovskite [32]. This issue can be solved by replacing PEDOT:PSS with an appropriate HTM, which has better energy band alignment such as poly-TPD or PTAA. As can be seen in the band diagram, the valance band (VB) energy level of PTAA (-5.2 eV) is closer to the perovskite VB level (-5.4 eV) compared with that of PEDOT:PSS (-5.0 eV). This results in a larger quasi-Fermi level separation and a smoother pathway for the hole transport, which in turns increase the *V*oc.

In this study, we also propose a modified inter-diffusion method to grow the perovskite film. The fabrication details can be found in the Experimental Section. We modified the conventional method by spin-coating hot, high-concentration, MAI solution on PbI_2 to initiate the reaction and this lasts for 2 min to pre-crystalize the perovskite film before the solvent-assisted annealing. There is a tradeoff between the perovskite layer thickness (over 400 nm) and the thickness of the PbI_2 residue in the conventional method [31]. We have devoted much effort to optimize the recipe of the modified inter-diffusion method in order to overcome the difficulty of fully consuming PbI_2 layer. Fig. 2(c) shows the XRD pattern of the grown $MAPbI_3$ film on an FTO substrate after annealing. The red curve is the XRD pattern of PbI_2 film, which has a strong peak on its (001) plane. The black curve indicates the XRD pattern of the $MAPbI_3$ film. There are no PbI_2 peaks present compared with the red curve, which reveals the full consumption of the PbI_2 layer. We note that there are some common peaks to both PbI_2 and $MAPbI_3$, which belongs to the FTO substrate. Fig. 2(d) illustrates the cross-sectional SEM image of a single perovskite thin film grown on the FTO/PTAA surface. The average thickness of the perovskite layer is about 450 nm with clear tight grain boundaries and lateral grain sizes over 1.0 μm.

The perovskite layer is grown directly on the PTAA thin film. The small amount of m-MTDATA additive (10 wt% ratio of PTAA) in the PTAA solution plays an important role to modify the non-wetting PTAA surface, enabling full film coverage of the PbI_2 layer. On the other hand, it is found by Huang that the grain size of perovskite is highly dependent on the hydrophobicity of the bottom layer surface [27]. With the help of surface modification by m-MTDATA additive, the PTAA-based perovskite grain size is greatly enlarged compared with that of PEDOT:PSS-based perovskite. Fig. 3 shows the SEM images of perovskite crystals grown on PEDOT:PSS and PTAA separately, and their corresponding grain sizes distribution histogram. It can be clearly seen that the perovskite grain sizes in Fig. 3(a) are smaller than in Fig. 3(b). The average grain size is 528 nm for the PEDOT:PSS-based perovskite crystals, and 850 nm for the modified PTAA-based perovskite crystals using the same growth conditions.

The PTAA's doping level directly modifies the film resistivity and affects the series resistance of the device. Huang *et al.* have reported to use a PTAA:F4-TCNQ blend solution with

TABLE I
PARAMETERS OF PEROVSKITE SOLAR CELL SAMPLES USING PTAA EXPOSED WITH VARIOUS DOPING CONCENTRATIONS

Doping Concentration	Voc (V)	Jsc (mA/cm2)	FF (%)	PCE (%)	Rs (ohm*cm2)
0	0.91	20.7	52.4	9.9	11.6
0.1 mg/ml	0.97	21.6	67.6	14.2	6.2
0.5 mg/ml	0.96	21.4	70.5	14.5	5.2
1.0 mg/ml	1.00	22.1	68.8	15.3	4.8
2.5 mg/ml	0.94	19.7	58.5	10.9	9.8
Reference	0.98	18.8	68.8	12.7	5.1

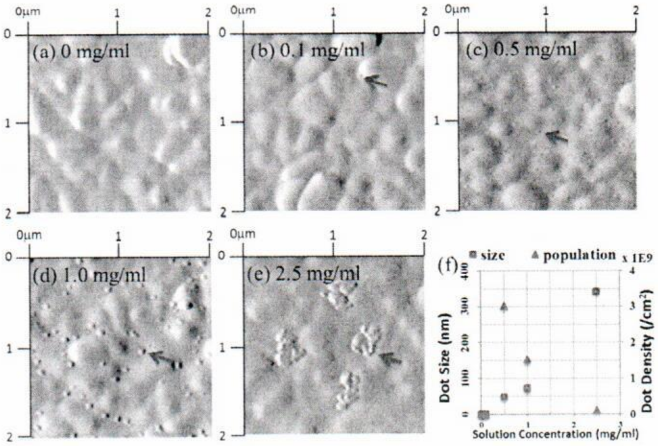

Fig. 4. AFM image of PTAA surface exposed with (a) 0 mg/ml, (b) 0.1 mg/ml, (c) 0.5 mg/ml, (d) 1.0 mg/ml, (e) 2.5 mg/ml, and (f) summarized doping size and density chart of the corresponding PTAA surface.

different doping ratios from 0 wt% to 10 wt%, and claimed that the 1 wt% doping ratio performs the best with a lower series resistance [28]. While it has been reported that polymer: F4-TCNQ blend solution requires diluted concentration and high temperature to suppress the doping particle aggregation [30], we also observed the degradation of F4-TCNQ in blend toluene solution. These drawbacks deteriorate the reproducibility and stability of the device performance. It is important to re-prepare the blend solution frequently to avoid using degraded/aggregated solution. Even though we may exclude any uncertainties for each blend solution preparation such as the doping ratio and the solution concentration variation, the dosage of PTAA, m-MTDATA, and F4-TCNQ increases remarkably. The cost of solar cell fabrication is greatly raised since the unit prices of PTAA and F4-TCNQ are more than 10 times the price of gold. In our study, we propose a sequential method to dope PTAA thin films in order to minimize the drawbacks of PTAA:F4-TCNQ blend solutions. We find that F4-TCNQ is soluble in 2-propano but the PTAA's solubility is very poor. Thus, we prepare the PTAA and the m-MTDATA in toluene and the F4-TCNQ in 2-propanol. We then spin-coat the PTAA first and then expose the PTAA thin film in a F4-TCNQ solution for 30 s before spinning the rest of the solution away. The PTAA's doping level can be tuned with the concentration of F4-TCNQ solution. We varied the PTAA's doping level using the sequential doping method and investigated their corresponding solar cell's performance. We also prepared a reference sample based on Huang's best recipe of PTAA blend solution (1 wt% doping ratio). Table I summarizes the results obtained from five samples with sequentially doped PTAA and the reference sample. The corresponding series resistances are extracted by fitting their *I–V* curves with the following equation for each sample:

$$I = I_L - I_0 \exp\left(\frac{q\left(V + IR_s\right)}{nkT}\right) - \frac{V + IR_s}{R_{sh}}.$$

We can see that the series resistance decreases as the doping concentration increases from 0 to 1 mg/ml. It is attributed to the increased doping level in the PTAA thin film, which minimizes the PTAA's sheet resistance. The AFM images of the PTAA surface exposed with different doping solutions are shown in Fig. 4. We can clearly see the aggregated doping dots on the sample surface from Fig. 4(c)–(e), but the root-mean-square (rms) roughness of the corresponding PTAA films is almost the same and is around 13 nm. The dot size is increasing with the doping concentration. For PTAA doped with 2.5 mg/ml doping solution, enormous doping clusters are observed which result in larger effective sheet resistance of the PTAA film. This explains the abnormal increase of the series resistance of the solar cell sample exposed with 2.5 mg/ml doping solution. For the reference sample, we observed a slightly smaller *V*oc of 0.98 V but much smaller photocurrent of 18.8 mA/cm^2. While the FF and series resistance are comparable to our best sample with sequential doped PTAA, it turns out the sequential method could also achieve the optimized doping level of PTAA using the pristine blend PTAA solution.

Larger grain sizes reduce the grain boundaries and the interface traps, and long carrier diffusion lengths of the perovskite material enable better carrier transfer within the perovskite grains. As a result, larger perovskite grain sizes will improve the solar cell performance. In our study, the perovskite grain size and the pin-hole density can be finely controlled by tuning the solvent amount during the solvent-assisted annealing (SAA). Fig. 1(b) shows the set-up for the SAA that can precisely control the solvent vapor amount. Specifically, the same amount of solvent (DMF) is dropped on the four coverslips inside the large beaker, and the small beaker stands on the coverslips and leaves some space at the bottom to allow slow vapor exchange. The device is annealed inside the small beaker. It is observed that the solvent amount can affect the grain size of the perovskite crystals. Fig. 5(a) and (b) demonstrates the SEM images of the perovskite crystals annealed with different SAA conditions. Without solvent vapor, the average grain size of the perovskite crystals is 0.85 μm as previously shown in Fig. 3(b), while it is enlarged to 1.5 μm with 4 μl DMF SAA condition, and above 2.0 μm with 10 μl DMF SAA condition. We also observed the

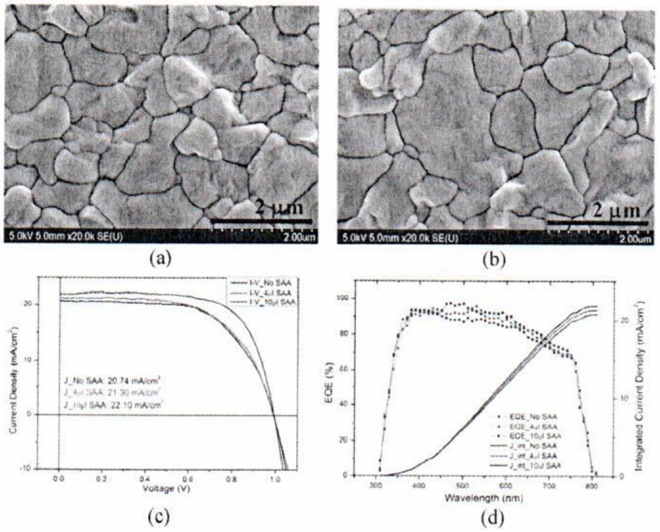

Fig. 5. SEM images of perovskite grains annealed with (a) 4 μl solvent and (b) 10 μl solvent during solvent-assisted annealing. (c) *I–V* performances of solar cells with No SAA, 4 μl SAA, and 10 μl SAA. (d) EQE comparison of the corresponding solar cells.

saturation effect of SAA on the grain size enhancement. Too much solvent during SAA would not improve the perovskite crystal quality, since the pin-hole density will keep increasing with the solvent amount. The optimization of the SAA condition is required to obtain high-quality perovskite crystals with a low pin-hole density and large grain sizes. The dependence of the solar cell performance on the SAA condition was investigated. Fig. 5(c) shows the *I–V* performances of three perovskite samples with 0, 4 and 10 μL solvent amount during SAA. The 10 μl SAA sample performs the best and exhibits the largest fill factor (FF) and short-circuit current (*J*sc). Fig. 5(d) shows the external quantum efficiency (EQE) of these samples and the integrated photocurrents are consistent with their *I–V* performances. The better performance of 10 μl SAA sample was contributed to its best perovskite crystal quality. Larger perovskite grain sizes provide better carrier transport within the perovskite layer with less recombination trap states. As a result, a larger photocurrent and EQE are observed in this sample. It is interesting to notice that the FF of the 4 μl SAA samples is even less than that of the 0 μl SAA sample. It is due to the increase of the pin-hole density that trades off the benefit of grain size enhancement, which provides more shunt-paths within the perovskite layer and reduces the shunt resistance of the device.

Fig. 6(a) shows the solar cell performance comparison between the PTAA and the PEDOT:PSS-based champion cell. The PTAA-based solar cell demonstrates an increase of the *J*sc from 19.8 to 22.1 mA/cm^2 and the *V*oc from 0.91 to 1.0 V. Though the FF decreases from 71% to 69%, the PCE of the PTAA-based solar cell reaches 15.3% compared with 12.7% from the PEDOT:PSS-based solar cell. The improved *V*oc is still less than the expected 1.1 V, which indicates the imperfect energy band alignment in our solar cell system. We thought that the defects at the PTAA/perovskite interface will introduce some trap states within the energy band, which in turn will lower down the work function of PTAA so that the electron-hole quasi-Fermi level separation decreases and *V*oc drops as a consequence. Further work is required to investigate this assumption and solve the issue. We also measured the EQE of the champion solar cells based on PTAA and PEDOT:PSS, respectively. As shown in Fig. 6(b), the EQE of the PTAA-based solar cell remains above 90% for the spectral range from 380 to 600 nm and then slowly drops to 80% at 680 nm, while the EQE of the PEDOT:PSS-based solar cell decays faster to 70% from 400 to 680 nm. The integrated photocurrent is 21.7 mA/cm^2 for the PTAA-based solar cell and 19.4 mA/cm^2 for the PEDOT:PSS-based solar cell, which are in good agreement with their measured short-circuit currents. The relatively low EQE in the region from 600 to 750 nm indicates the insufficienct perovskite thickness for both devices. We should further optimize our recipe to grow a thicker perovskite layer for a larger photocurrent and a higher power conversion efficiency.

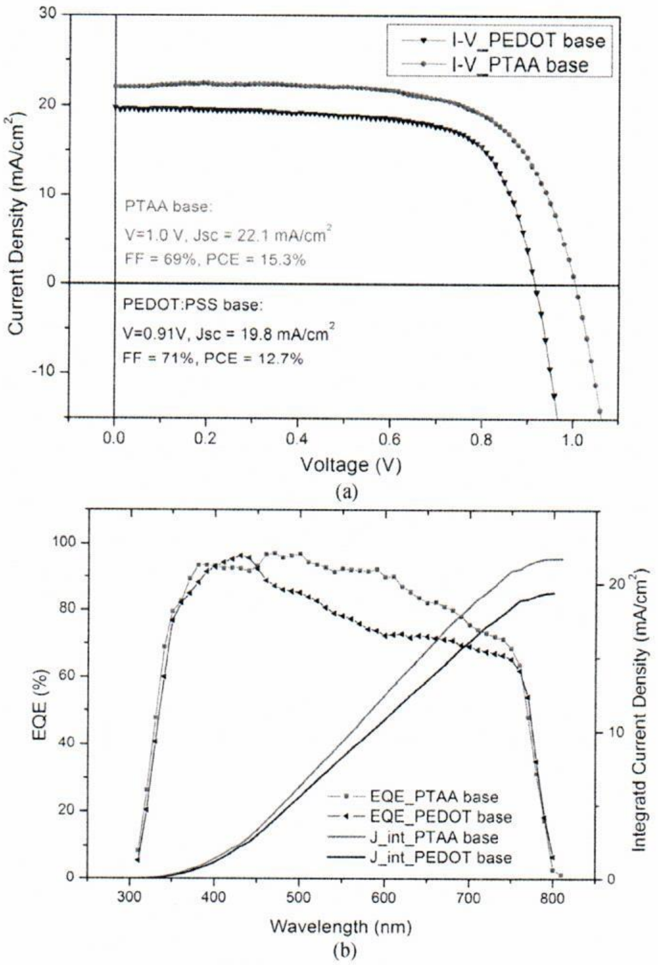

Fig. 6. (a) Photovoltaic performance comparison between champion cells with PTAA and PEDOT:PSS base. (b) EQE comparison between PTAA-based solar cell and PEDOT:PSS-based solar cell.

IV. CONCLUSION

In this study, we have proposed the sequential doping method to fabricate PTAA-based perovskite solar cell with simple inverted planar structure without any complicated surface passivation techniques. Compared with conventional PEDOT:PSS, PTAA increases the electron-hole quasi-Fermi separation so that the open-circuit voltage is remarkably improved. The sequential method provides an easier and more stable way to dope PTAA with F4-TCNQ in an orthogonal solvent base. The PTAA's doping level is tunable with the doping solution's concentration. It changes the PTAA film's sheet resistance and improves the solar cell's performance as a consequence. We have modified the inter-diffusion method for perovskite thin film growth in a controllable solvent-assisted-annealing set-up. We are able to grow high-quality perovskite crystals with grain sizes over 2 μm and thicknesses around 450 nm. The highest power conversion efficiency of 15.3% is obtained under AM1.5 irradiation. The measured photocurrent is consistent with the integrated photocurrent from the measured EQE data. However, the open-circuit voltage of 1.0 V is still below our expectation. We assume that the interface traps between the PTAA and the perovskite layers are the main cause for low Voc. More optimization is required to further improve the solar cell's performance.

ACKNOWLEDGMENT

The authors would like to acknowledge the support of the FabLab, AIMLab, and XCC facilities at the University of Maryland.

REFERENCES

[1] A. Kojima, K. Teshima, Y. Shirai, and T. Miyasaka, "Organometal halide perovskites as visible-light sensitizers for photovoltaic cells," *J. Amer. Chem. Soc.*, vol. 131, no. 17, pp. 6050–6051, 2009.

[2] Nrel.gov, 2019. [Online]. Available: https://www.nrel.gov/pv/assets/pdfs/pv-efficiency-chart.20190103.pdf. Accessed on: Jan. 11, 2019.

[3] Y. Sun, J. Peng, Y. Chen, Y. Yao, and Z. Liang, "Triple-cation mixed-halide perovskites: Towards efficient, annealing-free and air-stable solar cells enabled by $Pb(SCN)_2$ additive," *Sci. Rep.*, vol. 7, no. 1, 2017, Art. no. 46193.

[4] G. Xing *et al.*, "Long-range balanced electron- and hole-transport lengths in organic-inorganic $CH_3NH_3PbI_3$," *Science*, vol. 342, no. 6156, pp. 344–347, 2013.

[5] C. Motta, F. El-Mellouhi, and S. Sanvito, "Charge carrier mobility in hybrid halide perovskites," *Sci. Rep.*, vol. 5, no. 1, 2015, Art. no. 12746.

[6] J. Noh, S. Im, J. Heo, T. Mandal, and S. Seok, "Chemical management for colorful, efficient, and stable inorganic–organic hybrid nanostructured solar cells," *Nano Lett.*, vol. 13, no. 4, pp. 1764–1769, 2013.

[7] N. Jeon *et al.*, "Solvent engineering for high-performance inorganic–organic hybrid perovskite solar cells," *Nature Mater.*, vol. 13, no. 9, pp. 897–903, 2014.

[8] N. Jeon *et al.*, "Compositional engineering of perovskite materials for high-performance solar cells," *Nature*, vol. 517, no. 7535, pp. 476–480, 2015.

[9] W. Yang *et al.*, "High-performance photovoltaic perovskite layers fabricated through intramolecular exchange," *Science*, vol. 348, no. 6240, pp. 1234–1237, 2015.

[10] W. Yang *et al.*, "Iodide management in formamidinium-lead-halide–based perovskite layers for efficient solar cells," *Science*, vol. 356, no. 6345, pp. 1376–1379, 2017.

[11] D. Luo *et al.*, "Enhanced photovoltage for inverted planar heterojunction perovskite solar cells," *Science*, vol. 360, no. 6396, pp. 1442–1446, 2018.

[12] W. Chen *et al.*, "Efficient and stable large-area perovskite solar cells with inorganic charge extraction layers," *Science*, vol. 350, no. 6263, pp. 944–948, 2015.

[13] J. You *et al.*, "Improved air stability of perovskite solar cells via solution-processed metal oxide transport layers," *Nature Nanotechnol.*, vol. 11, no. 1, pp. 75–81, 2015.

[14] S. Ye *et al.*, "A breakthrough efficiency of 19.9% obtained in inverted perovskite solar cells by using an efficient trap state passivator Cu(thiourea)I," *J. Amer. Chem. Soc.*, vol. 139, no. 22, pp. 7504–7512, 2017.

[15] J. Christians, R. Fung, and P. Kamat, "An inorganic hole conductor for organo-lead halide perovskite solar cells. Improved hole conductivity with copper iodide," *J. Amer. Chem. Soc.*, vol. 136, no. 2, pp. 758–764, 2013.

[16] W. Chen *et al.*, "Molecule-doped nickel oxide: Verified charge transfer and planar inverted mixed cation perovskite solar cell," *Adv. Mater.*, vol. 30, no. 20, 2018, Art. no. 1800515.

[17] W. Chen *et al.*, "Understanding the doping effect on NiO: Toward high-performance inverted perovskite solar cells," *Adv. Energy Mater.*, vol. 8, no. 19, 2018, Art. no. 1703519.

[18] W. Chen *et al.*, "Cesium doped NiO x as an efficient hole extraction layer for inverted planar perovskite solar cells," vol. 7, 2019, Art. no. 1700722.

[19] J. Seo *et al.*, "Benefits of very thin PCBM and LiF layers for solution-processed p–i–n perovskite solar cells," *Energy Environ. Sci.*, vol. 7, no. 8, pp. 2642–2646, 2014.

[20] W. Nie *et al.*, "High-efficiency solution-processed perovskite solar cells with millimeter-scale grains," *Science*, vol. 347, no. 6221, pp. 522–525, 2015.

[21] J. You *et al.*, "Low-temperature solution-processed perovskite solar cells with high efficiency and flexibility," *ACS Nano*, vol. 8, no. 2, pp. 1674–1680, 2014.

[22] S. Sun *et al.*, "The origin of high efficiency in low-temperature solution-processable bilayer organometal halide hybrid solar cells," *Energy Environ. Sci.*, vol. 7, no. 1, pp. 399–407, 2014.

[23] P. Liang, C. Chueh, S. Williams, and A. Jen, "Roles of fullerene-based interlayers in enhancing the performance of organometal perovskite thin-film solar cells," *Adv. Energy Mater.*, vol. 5, no. 10, 2015, Art. no. 1402321.

[24] D. Zhao *et al.*, "High-efficiency solution-processed planar perovskite solar cells with a polymer hole transport layer," *Adv. Energy Mater.*, vol. 5, no. 6, 2015, Art. no. 1401855.

[25] O. Malinkiewicz *et al.*, "Perovskite solar cells employing organic charge-transport layers," *Nature Photon.*, vol. 8, no. 2, pp. 128–132, 2013.

[26] X. Xu *et al.*, "Ultraviolet-ozone surface modification for non-wetting hole transport materials based inverted planar perovskite solar cells with efficiency exceeding 18%," *J. Power Sources*, vol. 360, pp. 157–165, 2017.

[27] C. Bi *et al.*, "Non-wetting surface-driven high-aspect-ratio crystalline grain growth for efficient hybrid perovskite solar cells," *Nature Commun.*, vol. 6, no. 1, 2015, Art. no. 7747.

[28] Q. Wang, C. Bi, and J. Huang, "Doped hole transport layer for efficiency enhancement in planar heterojunction organolead trihalide perovskite solar cells," *Nano Energy*, vol. 15, pp. 275–280, 2015.

[29] X. Zheng *et al.*, "Defect passivation in hybrid perovskite solar cells using quaternary ammonium halide anions and cations," *Nature Energy*, vol. 2, no. 7, 2017, Art. no. 17102.

[30] I. Jacobs *et al.*, "Comparison of solution-mixed and sequentially processed P3HT:F4TCNQ films: Effect of doping-induced aggregation on film morphology," *J. Mater. Chem. C*, vol. 4, no. 16, pp. 3454–3466, 2016.

[31] Z. Xiao *et al.*, "Efficient, high yield perovskite photovoltaic devices grown by interdiffusion of solution-processed precursor stacking layers," *Energy Environ. Sci.*, vol. 7, no. 8, pp. 2619–2623, 2014.

[32] W. Yin, L. Pan, T. Yang, and Y. Liang, "Recent advances in interface engineering for planar heterojunction perovskite solar cells," *Molecules*, vol. 21, no. 7, 2016, Art. no. E837.